A novel photoresponsive ZnO-flyash nanocomposite for environmental and energy applications

A.N. Ökte [a],[*], D. Karamanis [b],[**]

[a] Department of Chemistry, Boğaziçi University, Bebek 34342, Istanbul, Turkey
[b] Department of Environmental & Natural Resources Management, University of Ioannina, 30100, Agrinio, Greece

ABSTRACT

ZnO nanoparticles were in situ synthesized on lignite fly ash (ZnO-FA) characterized and tested for the degradation of methyl orange (MO) and water vapor adsorption toward evaporative cooling of hydrophilic surfaces. Surface area (BET) measurements of the supported catalysts revealed type IV adsorption isotherms with typical mesopores of 2–4 nm in their pore size distribution. The pore volume of the 0.25 M ZnO-FA was increased to $0.133\,cm^3\,g^{-1}$ from $0.009\,cm^3\,g^{-1}$ of the raw FA and $0.012\,cm^3\,g^{-1}$ of 0.25 M ZnO. In scanning electron microscopy (SEM) images the non-shaped ZnO aggregates existed either on the surface of the FA spheres or heterogeneously dispersed over the whole catalyst matrix. X-ray photoelectron spectroscopy (XPS) confirmed the buildup of ZnO nanoparticles while the form of Zn^{2+} oxidation state on the catalyst surface was demonstrated by the sharp Zn $2p_{3/2}$ peaks. The absorption edges in the UV–vis diffuse reflectance spectra (UV–vis DRS) of all supported catalysts were found to be slightly shifted to longer wavelength regions due to the existence of FA in the composite structure. Moreover, the mesoporous ZnO-FA was hydrophilic with capillary condensation in the water vapor adsorption isotherm. Water vapor sorption was increased to $0.2\,g\,g^{-1}$ in the presence of 0.25 M ZnO-FA from $0.037\,g\,g^{-1}$ in the hydrophobic FA and 93% of relative humidity. In dark adsorption experiments, drastic decrements in the MO concentration in aqueous solutions were acquired by the implication of the ZnO-FA catalysts. This action was further enhanced under UV illumination with almost total MO photodegradation in less than 10 min with 0.5 M ZnO-FA. Thus, transformation of FA structure into a mesoporous adsorber with photocatalytic properties after the in situ ZnO growth is observed for the first time and widens the energy and environmental application prospects of coal residues.

© 2013 Elsevier B.V. All rights reserved.

1. Introduction

Sustaining and improving environmental quality represent one of the most important challenges. Pollution of water, air and soil is becoming an increasingly serious problem. Pollutants from diverse sources, pesticide and fertilizer runoff, abandoned industrial and mining sites, and airborne gaseous and particulate matter from automobiles exacerbate the situation on a daily basis. Detecting and treating existing contaminants and preventing new pollution are among the challenges.

In this direction, heterogeneous semiconducting oxide-based photocatalysis is being intensely examined from both fundamental and practical perspectives. Research efforts have been expanded from the environmental remediation scenarios to the broader

applications of the materials used in the photocatalysis [1]. TiO_2 and ZnO are well known catalysts due to their unique ability in the environmental applications [2–5]. In the past few years, ZnO has attracted much attention because of its distinctive optoelectronic, low cost, catalytic and photochemical properties [6,7,4,8]. In some cases, ZnO has revealed higher activities than TiO_2 owing to the smaller particle sizes and better dispersion [9,10]. Moreover, ZnO functions in a larger fraction of UV spectrum while its nanostructure can be attained at low temperature [11]. However, ZnO is not stable in acidic or alkaline conditions and also show rapid deactivation in bulk due to increased tendency of aggregation which eventually reduces the light incidence [11]. In addition, poor adsorption capacity (by being non-porous), the low surface area and recycling difficulties owing to long time centrifugation or sedimentation processes restrict the utilization of bare semiconductors in photocatalytic reactions. Thus, supported catalyst systems are generated by using porous adsorbent materials. Among these materials, silica [12], alumina [13], activated carbon [14,15], zeolites [16–20], clays [21,22] and MCM [23] are commonly used ones. Higher specific surface areas and more effective adsorption

* Corresponding author. Tel.: +90 212 359 7390; fax: +90 212 287 2467.
** Corresponding author. Tel.: +30 26410 74210; fax: +30 26410 39576.
E-mail addresses: okteayse@boun.edu.tr (A.N. Ökte), dkaraman@cc.uoi.gr
(D. Karamanis).

sites are being elucidating advantages of using supported catalysts. The enhanced degradation rates can be attributed to the increased condensation of pollutants on the supported catalysts by adsorption and the reduced electron–hole recombination process on the surface [24]. Obviously, cost reduction with the selection of an abundant and inexpensive matrix with complementary adsorption properties is of primary importance.

In addition, chemical pollution in the urban environment is strongly connected with the thermal pollution or the so called heat island effect (temperature increase within cities) [25]. The urban heat island is an environmental problem that results in unfavorable conditions for human health and increases in energy consumption due to the increased cooling demand. Recently, it has been proposed that by using porous materials to cover buildings surface, it is possible to lower the surface temperature by utilizing full or part of the cycle of water vapor adsorption-condensation-evaporation-desorption thermal energy properties [26,27]. It has been found that the latent heat released from stored moisture during rain, or absorbed moisture during high humidity at night, will lower surface temperatures like in the roof during daylight hours. By supporting the catalyst on hydrophilic porous materials, different parts of the solar spectrum could be utilized for simultaneous multifunctional purposes (like UV–vis for photodegradation and IR for providing the thermal energy for phase changes) and nanocomposites could be applied for combined processes like solar cooling in addition to pollutants photodegradation.

Fly ashes (FA) are aluminosilicate-rich by-products generated in coal firing powder plants. They are unique, non-toxic, chemically and physically stable, abundant and cheap, low density hollow particles [28]. They can be beneficially used in the building industry and road construction applications such as cement or asphalt additive, autoclaved aerated concrete block, concrete admixture, highway ice control, and hazardous waste removal. In spite of these applications, the large quantities produced by industry create environment and waste management issues. Therefore, the development of alternative potential applications and further means to facilitate the recycling of incineration ashes are urgently needed. In these circumstances, fly ash cenospheres can be utilized for the evaluation of water vapor adsorption capacity and suitability to lower the surface temperature under irradiation.

Moreover, fly ash materials were used as substrates in the studies of Lu et al. [29] and Liu et al. [30]. Recent investigations have been focused on the TiO$_2$ supported fly ash catalytic systems. Yu reported that coal fly ash coated with 10 wt% TiO$_2$, formed 9 nm sized anatase crystals and showed 63% and 67.5% NO removal rates at 300 °C and 400 °C, respectively [31]. Visa et al. observed an improved adsorption of cadmium and copper ions in the presence of 25% TiO$_2$ associated fly ash mixture [32]. Fly-ash cenospheres were used as carriers for the floating photocatalyst system of cobalt sulfophtalocyanine sensitized TiO$_2$ sol samples [33]. This system presented a good activity through degradation of methylene blue up to a certain extent of cobalt sulfophtalocyanine. In another study, a series of poly-o-phenylenediamine/TiO$_2$/fly-ash composites were synthesized, characterized and tested for the degradation of antibiotics in waste water under visible light [34]. At pH 3 and polymerization time of around 40 min, 60% degradation rate of roxithromycin was achieved by indicating the viability of the prepared composites. H$_2$O$_2$ modified TiO$_2$ loaded fly ash systems exhibited an enhanced performance for the degradation of methylene blue [35]. Another study examined the effect of TiO$_2$ loading method (sol–gel, ambient hydrolysis and hybrid slurry) on the surface of a coal fly ash sample to follow depigmentation and mineralization of methyl orange under ultraviolet-visible irradiation [36]. 94.96% photodegradation of Rhodamine B was achieved in 180 min under visible light irradiation in the presence of floating photocatalysts of fly-ash cenospheres supported AgCl/TiO$_2$ films [37]. The

effect of calcination temperature and loading percent of TiO$_2$ on the structural property and photocatalytic activity of TiO$_2$ immobilized coal fly ash samples were investigated in detail by using methyl orange as a model pollutant [38,39]. 94.35% of phenol removal was obtained in four hours irradiation time in the presence of TiO$_2$ supported fly ash [40]. The photocatalytic activity and kinetics of Fe^{3+} doped TiO$_2$ film deposited on fly ash cenosphere were investigated by measuring the photodegradation of methyl blue [41]. It was found that addition of iron ions increased the degradation efficiency by 33% with 450 °C calcined composite. The polypyrrole sensitized TiO$_2$ layer on fly ash cenosphere was prepared as a promising catalyst in the study of Wang et al. [42]. They noticed the best catalytic performance for the degradation of phenol and methyl blue with a Py/Ti ratio of 1% in the presence of 1 mol L^{-1} HCl.

Although TiO$_2$-fly ash systems were examined in detail, to the best of our knowledge, ZnO-fly ash composites were not studied before. Thus, the objective of the present study is to prepare ZnO photocatalysts supported on fly ash materials. This is followed by exploring their bifunctional applications for the degradation of a model pollutant and for the evaporative cooling of hydrophilic surfaces. In this direction, the ZnO catalysts are in situ synthesized on FA particles at different initial concentrations. Characterizations of the supported catalysts are carried out by using several techniques such as elemental analysis, X-ray diffraction (XRD), nitrogen adsorption desorption isotherms (BET), scanning electron microscopy with energy dispersive spot analysis (SEM-EDX) and/or elemental mapping, X-ray photoelectron spectroscopy (XPS) and UV–vis diffuse reflectance spectra (UV–vis DRS). The materials are evaluated for the moisture sorption on fly ash with or without ZnO buildup. Decolorization and degradation of MO is followed under UV illumination in the presence of the as prepared catalysts. Kinetics of the photodegradation reaction is investigated by following Langmuir–Hinshewood model. Besides, recycling studies are performed to test the repeatability of the photocatalysts.

2. Experimental

2.1. Materials

Fresh lignite by-products of fly ashes, coded FA, were obtained from the major lignite power plant of Greece. Fly ash was collected in a dry state from the electrostatic precipitators of the power station. All samples were ground by hand and sieved to a fragment size less than 200 μm. Zinc nitrate hexahydrate (Zn(NO$_3$)$_2$·6H$_2$O) (99.0%, Merck), sodium carbonate (Na$_2$CO$_3$) (Analytical Grade, Merck), [4-[[(4-dimethylamino)phenyl]-azo]benzenesulfonic acid sodium salt] (methyl orange, Merck) were used as provided by the suppliers without further purification. All chemicals were used as provided by the suppliers without further purification. Deionized water, purified with an Elga-Pure Water Purification (UHQ II) system, was used for preparing solutions in the experiments.

2.2. Preparation of the photocatalysts

ZnO catalysts in the absence of the support FA were prepared by a coprecipitation method using Zn(NO$_3$)$_2$·6H$_2$O and Na$_2$CO$_3$ precursors as described in the study of Anandan et al. [43]. The precursors with certain concentrations (0.125 M, 0.25 M and 0.5 M) were separately dissolved in deionized water. Then, 100 mL of Zn(NO$_3$)$_2$·6H$_2$O were slowly added into vigorously stirred 100 mL of Na$_2$CO$_3$ solution. The resulting white suspension was agitated by magnetic stirrer for 2 h at room temperature. This step was followed by several centrifugations at 4000 rpm and washings with

deionized water. Then, the catalysts were dried at $100\,^\circ C$ for 12 h. The calcination step was done in a muffle furnace using ambient air at $500\,^\circ C$ with a heating rate of $10\,^\circ C\,min^{-1}$ for 5 h. In this, in situ growth of ZnO particles was achieved. Finally, the catalysts were ground into fine powder, stored in dark and named as 0.125 M ZnO, 0.25 M ZnO and 0.5 M ZnO.

Supported catalysts were prepared with the addition of 2 g FA suspended in water (about 2 h) into the precursor's 200 mL solution. The same precursor concentrations were used as mentioned above. After stirring the mixed suspension about 12 h at room temperature, several centrifugations (at 4000 rpm) and washings were applied. The resulting supported catalysts were dried at $100\,^\circ C$ for 12 h and then, calcined in a muffle furnace using ambient air at $500\,^\circ C$ with a heating rate of $10\,^\circ C\,min^{-1}$ for 5 h. Finally, the catalysts were ground into fine powder, stored in dark and named as 0.125 M ZnO-FA, 0.25 M ZnO-FA and 0.5 M ZnO-FA. The color of the supported catalysts changed from dark yellowish gray to bright gray depending on the concentration of the ZnO loaded.

The supported catalyst (0.25 M ZnO-FA) stability was controlled by means of Zn concentration in solution using a Varian Spectraa 250 Plus atomic absorption spectrophotometer, equipped with a hollow cathode lamp (214 nm). Three sets of experiments were done. Zn concentration was found as $0.007\,mg\,L^{-1}$ in the solution of 0.25 M ZnO-FA and de-ionized water (stirred in the dark about 30 min), $0.009\,mg\,L^{-1}$ in the solution of 0.25 M ZnO-FA and $3.27\,mg\,L^{-1}$ MO (stirred in the dark about 30 min) and $0.859\,mg\,L^{-1}$ in the solution of 0.25 M ZnO-FA and $3.27\,mg\,L^{-1}$ MO (stirred under irradiation about 30 min). Based on our XRF measurements, 0.25 M ZnO-FA has about 24 wt% of Zn. Since in photocatalytic runs (Section 2.4), 0.1 g of catalyst was used in 100 mL solution, the amount of Zn corresponded to $240\,mg\,L^{-1}$. Thus, the concentrations of Zn found in the above mentioned solutions were assumed to be negligible under our experimental conditions.

2.3. Characterization techniques

The major chemical constituents and trace elements of the raw fly ash were determined with the spectrometric methods of X-ray fluorescence (XRF) and proton-induced gamma-ray emission (PIGE) [44]. PIGE measurements were carried out at the 5.5 MV terminal voltage of the Tandem accelerator of the National Center for Scientific Research "Demokritos", Greece. Characteristic γ-rays emitted from the deexcitation of the residual nuclei following $(p,p'\gamma)$ reactions, were used for the determination of light elements as Al, Si, Mg and Na. XRF measurements were performed by a vertical Si(Li) detector and a ring shaped radioisotope source (^{109}Cd or ^{241}Am) for providing the exciting radiation [44]. The X-ray powder diffraction (XRD) patterns of the 0.25 M ZnO and the supported catalysts were recorded on a Rigaku-D/MAX-Ultima diffractometer using Cu-Kα radiation ($\lambda = 1.54\,\text{Å}$) operating at 40 kV and 40 mA and scanning rate of $2^\circ\,min^{-1}$. The nitrogen adsorption/desorption isotherms were obtained at liquid nitrogen temperature of 77 K by using Quantachrome Nova 2200e automated gas adsorption system. The specific surface areas were determined by using multipoint BET analysis and the pores sizes were measured by the BJH method of adsorption. The surface morphologies of the FA before and after ZnO loading were determined by using scanning electron microscopy (SEM) in combination with energy dispersive X-ray analysis on an ESEM-FEG/EDAX Philips XL-30 instrument operating at 20 kV using catalyst powders supported on carbon tape. In X-ray photoelectron spectroscopy (XPS) tests, Thermo Scientific K-Alpha X-ray Photoelectron Spectrometer equipped with a hemispherical electron analyzer and Al-Kα micro-focused monochromator was used. The areas of peaks were estimated by calculating the integral of each peak after subtracting a Shirley background and fitting the experimental curve to a combination of Lorentzian/Gaussian

lines. The FTIR spectra were recorded on the Nicolet 380 FTIR spectrometer. The UV–vis diffuse reflectance spectra (UV–vis DRS) of the FA, 0.25 M ZnO and all supported catalysts obtained by using UV–vis spectrophotometer (UV-2450, Shimadzu) equipped with an integrating sphere reflectance accessory. The baseline correction was done by BaSO$_4$. The spectra were recorded in the range of 200–600 nm for all catalysts and the FA using BaSO$_4$ as reference. In the moisture sorption isotherms, samples were placed in desiccators with saturated salt solutions for controlling relative humidity (32.8, 57.6, 78.6 and 93.6%) while temperature was air-conditionally controlled at $25\,^\circ C$. Temperature and humidity inside the desiccators were continuously monitored with a TFA Dostmann/Wertheim sensor. Prior to measurements, samples were dried to constant mass in an air-circulated oven at $105\,^\circ C$. In order to determine the sorption isotherms, the samples were periodically weighed and the moisture content was calculated as the difference of mass measurements in different time periods and the initial dry state.

2.4. Photocatalytic experiments

For all degradation experiments, a pyrex Erlenmeyer flask was used as a reactor and located in a laboratory constructed "irradiation box", equipped with eight black light lamps (Philips TL 15W/5BLB) of wavelength 320–440 nm. The incident photon flux for all lamps was measured as 4.7×10^{15} photons/s using an actinometric method based on the photochemical decomposition of $K_3Fe(C_2O_4)_3$ complex. Heating effect of the lamps was eliminated by a fan, placed at one end of the box. The reactor was containing an inlet for the circulation of air (provided by a Cole-Palmer peristaltic pump) and an outlet for the collection of aliquots. All experiments were performed in continuous circulation mode; aliquots (about 5 mL) were retrieved from the outlet at certain time intervals and analyzed after filtering through Millipore filter (0.45 μm). MO, selected as the model compound, is a water soluble azo dye. Like many other dyes of its class MO can enter the body through ingestion and the high content in living systems can prove to be carcinogenic [45,46]. According to Galindo et al. [47], concentrations of MO in the range of 32.7–$0.327\,mg\,L^{-1}$ were commonly found in textile effluents. Based on this study, $3.27\,mg\,L^{-1}$ stock solution of MO was prepared by dissolving the required amount in deionized water unless concentration effect of MO was tested. Reaction systems were set-up by adding 0.1 g of catalysts into 100 mL of MO known concentration in aqueous media at room temperature. Prior to illumination, to ensure the equilibrium of dark adsorption process, suspensions were magnetically stirred for 2 min in the presence of the supported catalysts and 30 min in the presence of 0.125–0.5 M ZnO catalysts. UV–vis spectrophotometer (UV-2450, Shimadzu) was used to monitor the absorbance spectra of MO as a function of illumination time. The absorbance at 274 nm represented the aromatic content of MO and the decrease of the band at this wavelength indicated degradation of MO's aromatic moiety. The absorbance at 464 nm was due to the color of MO solution and it was used to examine the decolorization of MO solution. All experiments were performed at room temperature and at pH = 8 ($3.27\,mg\,L^{-1}$ MO in the presence of 0.25 M ZnO-FA) without concerning the degradation intermediates. Also, measurements were conducted at least twice and the average value was recorded. The degradation and decolorization rate percentages of MO were calculated by the following equation:

$$\text{Degradation (or Decolorization) }(\%) = \frac{C_0 - C}{C_0} \times 100 \tag{1}$$

where C_0 is the initial concentration of MO and C is the concentration of MO after "t" minutes UV irradiation.

Table 1
Elemental compositions of FA, 0.25 M ZnO, 0.25 M ZnO-FA and 0.5 M ZnO-FA catalysts as bulk materials or at different SEM positions.

Materials	wt%								
	O	Mg	Al	Si	K	Ca	Ti	Fe	Zn
FA bulk[a]	43.7	3.4	8.7	20.0	1.9	22.4	0.2	3.0	0.004
FA (SEM sphere)	13.1	5.2	20.5	44.4	2.6	16.2	0.4	3.2	–
0.25 M ZnO[a]	26.5	–	–	–	–	–	–	–	73.5
0.25 M ZnO	14.2	–	–	–	–	–	–	–	85.8
0.5 M ZnO	24	–	–	–	–	–	–	–	75
0.25 M ZnO-FA (bulk)[a]	36.5	2.4	6.1	14.0	1.3	15.6	0.2	2.1	24.1
0.25 M ZnO-FA (whole SEM surface)	22.6	2.3	5.4	7.3	0.6	15.2	0.7	5.9	39.3
0.25 M ZnO-FA (right-top particle '1')	19.3	2.9	4.3	6.1	0.2	3.7	0.3	2.3	60.9
0.25 M ZnO-FA (right-bottom sphere '2')	26.1	6.5	10.5	15.4	0.6	14.6	1.1	7.1	18.0
0.25 M ZnO-FA (left-bottom sphere '3')	17.4	2.2	4.1	5.47	0.5	3.3	0.4	1.9	64.7
0.5 M ZnO-FA (bulk)[a]	33.2	1.9	4.9	11.2	1.0	12.5	0.2	1.7	35.3
0.5 M ZnO-FA (whole SEM surface)	15.7	1.8	2.9	3.7	0.3	3.1	0.2	3.1	69.3
0.25 M ZnO-FA (after dark adsorption)	14.4	1.5	3.9	5.4	0.5	3.1	0.4	2.9	67.8
0.25 M ZnO-FA (after 1st irradiation cycle)	21.9	2.1	4.5	6.7	0.4	4.1	0.5	2.6	57.2
0.25 M ZnO-FA (after 4th irradiation cycle)	23.7	2.2	5.1	7.8	0.6	3.9	0.3	2.9	53.2

[a] Results of XRF and PIGE measurements.

3. Results and discussion

3.1. Characterization of catalysts

3.1.1. Elemental analysis

During the combustion process, the burn-out of all combustible matter results in a significant enrichment of the ashes in incombustibles, which are partitioned between the bottom-ash (or slag), that falls inside the boiler, and the fly-ash that is suspended in the flue-gas together with vapors of volatile elements and compounds. Chemical analysis of the raw ash samples show that SiO_2 is the dominant oxide, with appreciable Al_2O_3 and CaO (Table 1). More than 90% of the composition of the studied sample consist of Si, Al, Fe and Ca oxides. Due to the high CaO content, the ashes are classified as Class C. The fly ash Si/Al ratio of 2.3 favors the treatment of the samples for the production of porous materials with large pore volume, high adsorption capacity and high ion-exchange capacity [48].

3.1.2. XRD analysis

XRD patterns of raw FA, 0.25 M ZnO and 0.125–0.5 M ZnO-FA catalysts are shown in Fig. 1. The support FA exhibits amorphous aluminosilicate glass (predominantly), quartz (SiO_2), gehlenite ($Ca_2Al_2SiO_7$), calcite ($CaCO_3$), lime (CaO), maghemite ($FeO \cdot Fe_2O_3$) and rankinite ($Ca_3Si_2O_7$) as minor crystalline structures at both low-angle ($2\theta < 10°$) and high-angle ($20° < 2\theta < 60°$) ranges (Fig. 1A).
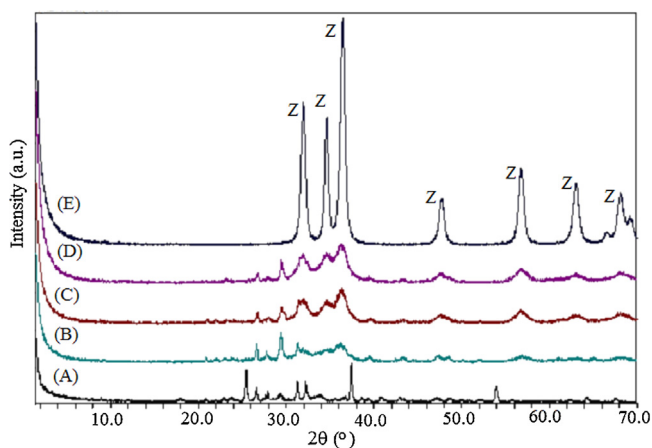

Fig. 1. XRD patterns of (A) FA, (B) 0.125 M ZnO-FA, (C) 0.25 M ZnO-FA, (D) 0.5 M ZnO-FA and (E) 0.25 M ZnO. (Z: ZnO).

Patterns of ZnO loaded FA catalysts exhibit wider and lower intense diffraction peaks than the raw FA (Fig. 1B–D). For 0.25 M ZnO, diffraction peaks indexed to d 1 0 0, d 0 0 2, d 1 0 1, d 1 0 2, d 1 1 0, d 1 0 3 and d 2 0 0 crystal planes of ZnO which appear at 31.9°, 34.6°, 36.4°, 47.7°, 56.7°, 63.1° and 66.6° (2θ), respectively (Fig. 1E). The characteristic peaks of FA and ZnO are retained in the supported catalysts indicating that the loading of ZnO does not influence the crystalline structure of both components. ZnO peaks are differentiated more clearly for the 0.25 M ZnO-FA than the 0.125 M ZnO-FA. However, signals are not intensified for higher ZnO concentrations (0.5 M ZnO-FA).

The crystalline sizes of ZnO nanoparticles, based on the broadening of the most intense (1 0 1) diffraction at 36.2° (2θ), were calculated by employing the Scherrer equation. The supported catalysts exhibit smaller crystalline sizes of ZnO nanoparticles in comparison to the non-supported form of ZnO catalyst (0.25 M ZnO) (Table 2). Besides, increase in the loading concentration of ZnO reduces the crystalline sizes as 11.56 nm, 9.67 nm and 8.12 nm for 0.125 M ZnO-FA, 0.25 M ZnO-FA and 0.5 M ZnO-FA, respectively. This may imply that hollow structure of the FA does not allow formation of ZnO aggregates. Although ZnO nanoparticles differ in dimensions, the decrements in the reflections of the raw support suggest their uniform distribution throughout the surface and bulk.

3.1.3. Nitrogen adsorption isotherms

A set of nitrogen adsorption–desorption tests were carried out for the raw FA, 0.25 M ZnO and 0.125 M-0.5 M ZnO-FA catalysts (Fig. 2a). Both the FA and 0.25 M ZnO exhibit Type II isotherms which refer to non-porous materials. However, supported nanocatalysts reveal Type IV isotherms with increases in nitrogen adsorption amounts as the pressure raised. Characteristic

Table 2
Crystalline sizes (D_{ZnO}), surface areas (BET), pore volumes (V_{pore}) and pore radius (r_{pore}) of 0.25 M ZnO, FA and the supported catalysts.

Materials	D_{ZnO} (nm)[a]	BET ($m^2\,g^{-1}$)[b]	V_{pore} ($cm^3\,g^{-1}$)[c]	r_{pore} (Å)[d]
0.25 M ZnO	16.08	7.58	0.012	17.75
FA	–	5.61	0.009	–
0.125 M ZnO-FA	11.56	30.81	0.067	14.80
0.25 M ZnO-FA	9.67	59.08	0.133	17.73
0.5 M ZnO-FA	8.12	60.15	0.122	16.69

[a] Calculated from the (1 0 1) diffraction peak of ZnO using the Scherrer equation.
[b] Determined from nitrogen adsorption–desorption isotherms using BET equation.
[c] Determined from cumulative adsorption pore volume using BJH method.
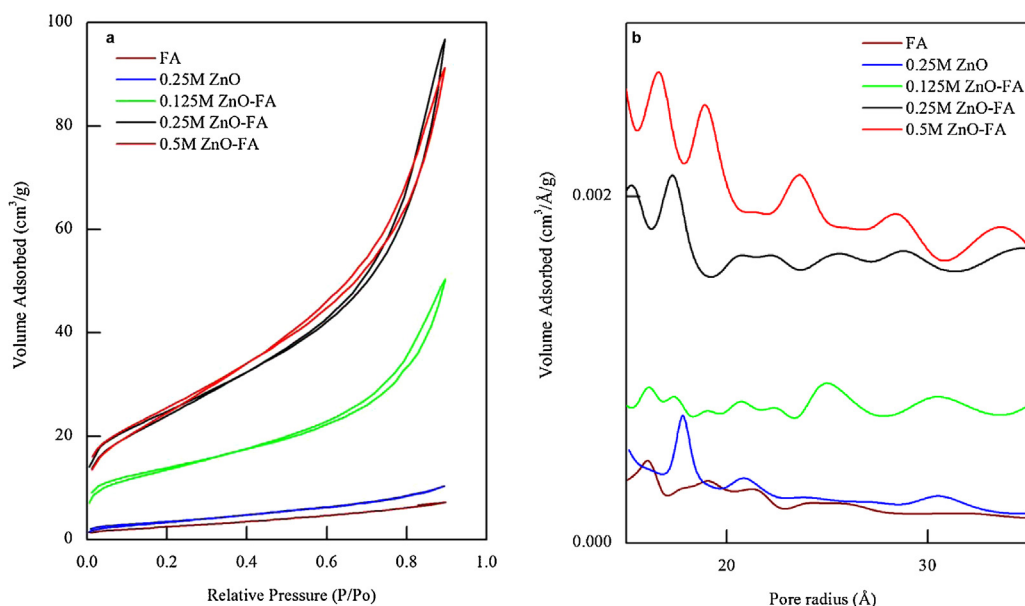[d] Determined from adsorption pore size using BJH method.

Fig. 2. BET surface area (a) and pore size distribution (b) plots for nitrogen adsorption/desorption on FA, 0.25 M ZnO, 0.125 M ZnO-FA, 0.25 M ZnO-FA and 0.5 M ZnO-FA.

feature of Type IV isotherm is its association with capillary condensation taking place in the mesopores in the range of high P/P_0 [49]. The pore size distribution curves display that the pores of the 0.125–0.5 M ZnO-FA catalysts are in typical mesoporous region of 2–4 nm (Fig. 2b). An inevitable increase is noticed in the pore volumes of the supported nanocatalysts, which results in higher surface areas relative to those obtained in the presence of the raw FA and 0.25 M ZnO (Table 2). Moreover, the largest area is achieved with the catalyst involving the highest concentration of ZnO. However, no noticeable difference is observed between 0.25 M and 0.5 M concentration of ZnO loadings, indicating the existence of a saturation effect at the 0.25 M ZnO concentration. This is consistent with the limited variation of the XRD peak intensities of the 0.25 M ZnO-FA and 0.5 M ZnO-FA catalysts. The decreasing trend in the crystalline sizes is in good agreement with the increasing surface area values of the supported catalysts.

3.1.4. SEM (EDX) analysis

Surface morphologies of the raw FA and 0.25 M ZnO-FA were investigated by SEM (EDX) analysis (Fig. 3). Raw FA shows two types of agglomerates: spherical and non-shaped particles (Fig. 3a). The spherical ones demonstrate varying morphologies. Some of them contain air holes on their surfaces (cenospheres) whereas the others are rather smooth without cracks and ridges or filled with smaller amorphous particles and crystals (plerospheres). The non-shaped aggregates exist either on the surface of the spheres or heterogeneously dispersed over the whole catalyst matrix. The EDX analysis of the SEM images revealed that particles of the raw FA are mainly composed of Si, Al and Ca (Table 1). Mg, K, Ti and Fe are also found as minor constituents. The ZnO nanoparticles in the image of 0.25 M ZnO are reasonably uniform in size and the morphologies takes on pseudo-spherical shape with detection of only Zn and O peaks in the EDX analysis (Fig. 3b and inset). For 0.25 M ZnO-FA, although spherical and non-shaped morphologies are retained, the appearance differs with the formation of non-uniform outer layers on top of these aggregates (Fig. 4). Vacancies noticed in Si, Al and Ca mappings of 0.25 M ZnO-FA are considered as probable adsorption sites of ZnO nanoparticles. This is evidenced in Zn mapping of the same catalyst which dominates Zn signal on top of the spheres and non-shaped particles (Fig. 4). Elemental compositions of the spherical aggregates labeled as 1, 2 and 3 in the image reveal different

Zn contents (Table 1). The surface morphology of 0.25 M ZnO-FA is further examined after dark adsorption of MO (Fig. S1), after 1st irradiation cycle (Fig. S2) and after 4th irradiation cycle (Fig. S3). The EDX analysis of these surfaces does not show a significant variation
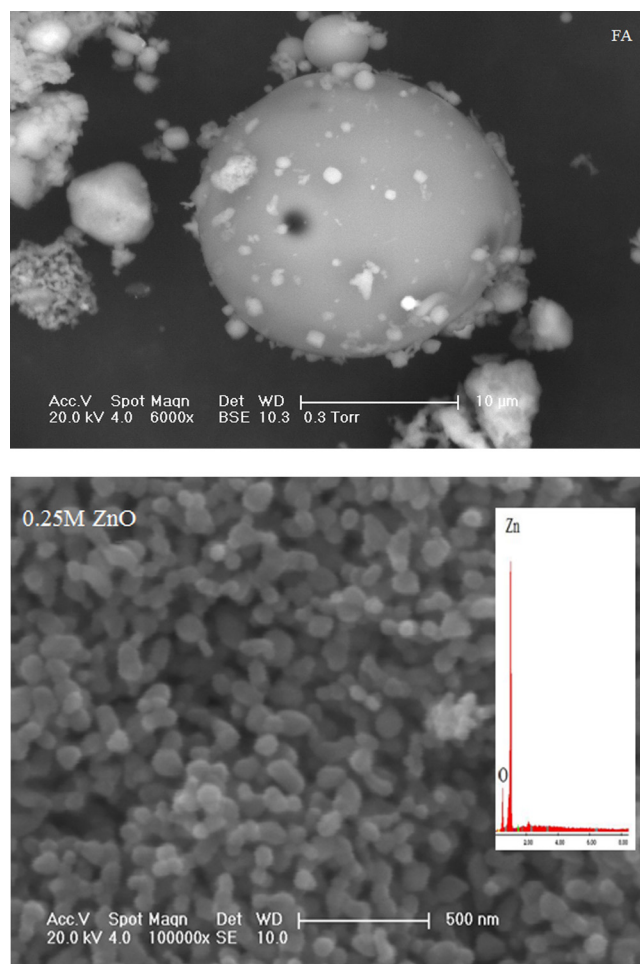

Fig. 3. SEM images of FA and 0.25 M ZnO (Inset: EDX analysis of 0.25 M ZnO).
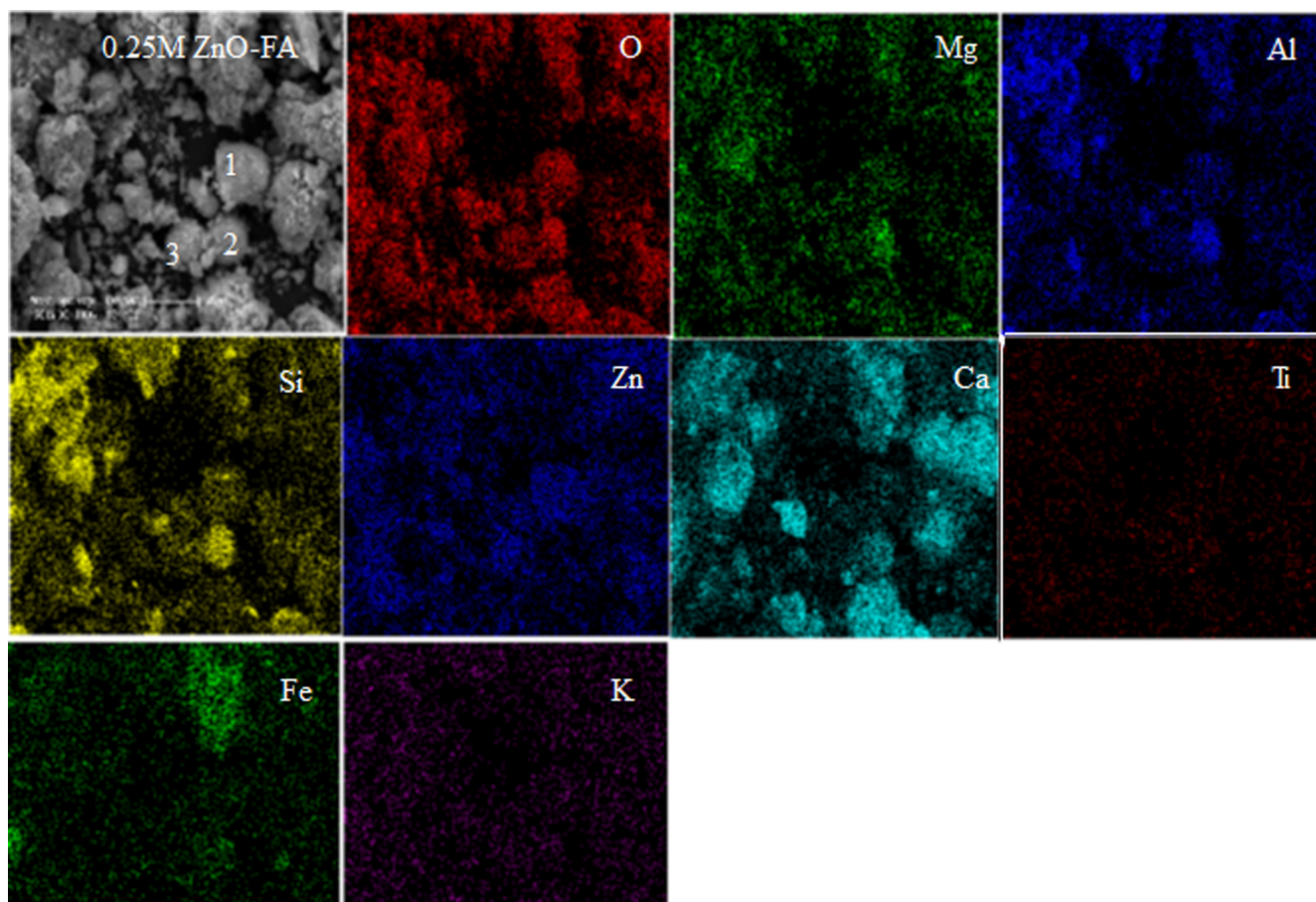
Fig. 4. SEM image of 0.25 M ZnO-FA. Images of elemental analysis: O, Mg, Al, Si, Zn, Ca, Ti, Fe and K mappings.

in the percentage of Zn, indicating the stability of the supported catalyst (Table 1).

3.1.5. XPS analysis

The surface composition and chemical states were further analyzed by means of XPS analysis based on the characteristic binding energies of different elements on material surfaces [50]. Accordingly, the XPS spectra of the raw FA, ZnO (Merck), 0.5 M ZnO and 0.5 M ZnO-FA were examined. Binding energy shifts are observed in all samples and hence, the instrument is calibrated using the carbon peak (C 1s) at 285 eV as in the other studies [51,52]. Also, ZnO (Merck) is used as a reference for the 0.5 M ZnO and 0.5 M ZnO-FA catalysts. Fig. 5 shows the XPS survey analysis for the raw FA, 0.5 M ZnO-FA, 0.5 M ZnO and ZnO (Merck). The raw FA reveals Al (75.6 eV) in the low binding energy regions (<100 eV), Si at 103 eV, C at 285 eV, Ca at 347.07 eV, Ti at 459 eV, O at 531.47 eV and some Auger peaks. For the supported catalyst, Zn peaks are clearly detected in the high binding energy regions and the intensities of the O and Ca peaks of the FA matrix considerably diminish, being in consistency with the corresponding XRD pattern. The similarities noticed in the full spectra of ZnO (Merck), 0.5 M ZnO and 0.5 M ZnO-FA confirm the presence of ZnO nanoparticles on the FA surface. Fig. 6 displays a doublet corresponding to Zn $2p_{3/2}$ and $2p_{1/2}$ core levels for ZnO (Merck), 0.5 M ZnO and 0.5 M ZnO-FA. The peak positions of Zn $2p_{3/2}$ and $2p_{1/2}$ of 0.5 M ZnO and 0.5 M ZnO-FA are quite similar to that of ZnO (Merck) (Table 3). Moreover, all Zn $2p_{3/2}$ peaks are sharp, demonstrating that Zn exists mainly in the form of Zn^{2+} oxidation state on the catalyst surfaces [50,53]. The O 1s spectra of the catalysts appear with wider and asymmetric peaks (Fig. 7). For the raw FA, the O 1s signal is deconvoluted by three subspectral

components: (i) A mixture of O 1s peak owing to the existence of MgO and TiO_2 species is observed in the original FA structure (529.11 eV, 17.8% spectral area) while the pure forms of MgO and TiO_2 possess O 1s peaks at 529.8 eV and 530 eV, respectively [54]. (ii) A combined form of O 1s peak is noticed due to CaO and Al_2O_3, the two main components of the FA composition (531.34 eV, 46.1% spectral area) while the O 1s original binding energies are at 531.5 eV and 531.1 eV for CaO and for Al_2O_3, respectively [54]. (iii) The O 1s peak is due to the presence of SiO_2, another main component of the FA matrix (532.78 eV, 36.1% spectral area) while pure SiO_2 has an O 1s signal at 532.5 eV [54]. The asymmetry in the O 1s peak for the ZnO (Merck) catalyst is explained by the deconvolution of two components to point out the presence of different oxygen species. These include the lattice oxygen of ZnO (O_L) with a binding energy of 529.98 eV and the chemisorbed oxygen (O_A) due to the surface hydroxyl groups with a higher binding energy (531.79 eV). Analogous deconvolutions are also used in the studies of Liqiang et al. [53] and Lai et al. [55]. The ZnO synthesized in this study (0.5 M ZnO) demonstrates quite similar binding energies for both O_L (529.98 eV) and O_A (531.67 eV). For 0.5 M ZnO-FA, O_L is shifted to 530.17 eV and O_A is detected at 531.63 eV. Binding energy values of Zn $2p_{3/2}$, Zn $2p_{1/2}$, O 1s and atomic number ratios of Zn $2p_{3/2}$ to $2p_{1/2}$, Zn $2p_{3/2}$ to total O and also Zn $2p_{1/2}$ to total O are given in Table 3 based on the following equation:

$$\text{Atomic ratio} = \frac{(\text{Peak area of the element}/\sigma \times \text{KE}^a)}{\sum(\text{Peak area of the element}/\sigma \times \text{KE}^a)} \quad (2)$$

where the element is Zn $2p_{3/2}$ or Zn $2p_{1/2}$ or O 1s, σ is the Scofield parameter of the corresponding element, and KE is the kinetic energy (=1486.6 − binding energy of the corresponding element).

Table 3
Binding energy (eV) values and atomic number ratios.

Catalysts	Zn 2p$_{3/2}$	Zn 2p$_{1/2}$	O 1s	Zn 2p$_{3/2}$ to 2p$_{1/2}$	Zn 2p$_{3/2}$ to total O	Zn 2p$_{1/2}$ to total O	Zn/O[a]
ZnO (Merck)	1021.20	1044.29	529.77	1.04	0.99	0.95	–
0.5 M ZnO	1021.20	1044.29	529.76	1.05	0.93	0.88	0.72[b]
0.5 M ZnO-FA	1021.20	1044.28	530.24	1.05	0.85	0.80	0.61[b]
							0.32[c]

[a] Mol ratios of Zn to O calculated from EDX data.
[b] An average in the overall surface scan.
[c] An average in the scan of spheres.

The form of the dependence of inelastic mean free path on KE is described by KE^a where "a" is equal to 0.7 [56].

The atomic number ratio of Zn 2p$_{3/2}$ to 2p$_{1/2}$ is found to be 1.04 for ZnO (Merck). The similar ratios obtained in the presence of 0.5 M ZnO (1.05) and 0.5 M ZnO-FA (1.05) indicates successful creation of ZnO nanoparticles in the synthesized materials. ZnO loading on the surface of the FA decreases the ratios of Zn 2p$_{3/2}$ to total O and Zn 2p$_{1/2}$ to total O. This suggests that the total content of surface oxygen species in the supported catalyst is larger than that of ZnO (Merck) and 0.5 M ZnO. Table 4 shows the O 1s curve fitting values of the catalysts. 0.5 M ZnO-FA reveals a decrement in the O$_L$ percentage (which suggests formation of more oxygen deficiencies in the ZnO lattice) and an increment in the O$_A$ percentage (which suggests adsorption of more OH groups). It is expected that the deficiency generated in the oxygen content of the 0.5 M ZnO-FA is compensated by the increase in the number of more surface bounded OH groups. These OH groups are responsible for the increase of the water vapor adsorption in the semiconducting composites from the raw fly ash, while promoting the formation of OH$^\bullet$ radicals via photoinduced holes. The photocatalytic degradation reactions can be facilitated with the subsequent attacks of highly active OH$^\bullet$ radicals to model moieties [53]. Thus, it is concluded that the ZnO addition to the FA matrix can enhance both the photocatalytic performance and the water vapor adsorption ability owing to the increase in the content of the surface OH groups. Moreover, since XPS analyses the outer surfaces, the obtained higher Zn to O ratio suggests the attachment of ZnO nanoparticles on the FA surfaces (mainly cenospheres) for the supported catalyst, in consistency with the SEM images. The relatively lower values obtained in the EDX analysis signifies the dominance of O also in the deep sites of the 0.5 M ZnO and 0.5 M ZnO-FA catalysts. For 0.5 M ZnO-FA, the decrease in the Zn to O ratio, either on the overall surface analysis or in the analysis of the spheres, results in the increment of total O content. This may initiate an alternative degradation route via photoinduced electrons to favor generation of superoxide radicals and then OH$^\bullet$ radicals.

3.1.6. FTIR analysis

Fig. 8 shows FTIR spectra of MO, FA, 0.25 M ZnO-FA, 0.25 M ZnO-FA (after 30 min dark adsorption), 0.25 M ZnO-FA (after 1st irradiation cycle) and 0.25 M ZnO-FA (after 4th irradiation

Table 4
O 1s curve fitting results.

Catalysts		O$_L$	O$_A$
ZnO (Merck)	E_b (eV)	529.98	531.79
	[a]Area (%)	74	26
0.5 M ZnO	E_b (eV)	529.98	531.67
	[a]Area (%)	75	25
0.5 M ZnO-FA	E_b (eV)	530.17	531.63
	[a]Area (%)	68	31

[a] The percent of O$_L$ or O$_A$ to the total oxygen.

cycle). MO display a peak at 2900 cm^{-1} for asymmetric −CH$_3$ stretching vibrations and another peak at 1599 cm^{-1} for −C=C− stretching (Fig. 8A). The peak at 1519 cm^{-1} is associated to the azo-chromophore and the one at 1417 cm^{-1} is due to the C=C−H in plane C−H bending. Other characteristic MO peaks appear at 1313 cm^{-1} for the −C=N stretching, 1119 cm^{-1} for the −S=O stretching, 1040, 1007 and 838 cm^{-1} for ring vibrations and 816 cm^{-1} for disubstituted benzene ring. FA shows characteristic bands near about 873 and 1110 cm^{-1} (Fig. 8B). The former corresponds to Si−O−Si symmetrical stretching vibration and the latter can be assigned to Si−O−Si and Al−O−Si asymmetric stretching vibrations. Besides, Si−O stretching of Si−OH and Si−O$^-$ groups appears at around 965 cm^{-1}. The band at 1409 cm^{-1} is attributed to stretching vibrations of CO$_x$ surface species (CO$_2^-$, CO$_3^{2-}$, HCO$_3^-$) due to the presence of calcite in the raw FA and the atmospheric carbonation carried to the surface structure of the support during the analysis [57]. No shifts of the FA characteristic IR bands are noticed after loading with ZnO nanoparticles, indicating creation of the supported nanocatalyst system via van der Waals interactions (Fig. 8C). Such interactions were also reported in the TiO$_2$ deposited fly ash materials [42]. In the meantime, 0.25 M ZnO-FA catalyst reveals complete disappearance of the peak at 1110 cm^{-1}, demonstrating the association of Si−O−Si and Al−O−Si bonds with ZnO nanoparticles and the creation of Si−OH groups. In the same context, the intensity of the peak at 873 cm^{-1} is also reduced. The broadness at 3400 cm^{-1} at the composites can be assigned to Si−OH bond vibration. The bending peak at around 1650 cm^{-1} is due to the presence of surface hydroxyls and coordinated water molecules. The IR pattern of the supported catalyst does not vary after MO dark adsorption and also after the first and fourth irradiation cycles (Fig. 8D–F). The intensity of the broad band at around 3400 cm^{-1} is becoming higher after each irradiation cycle due to higher adsorption of water molecules. MO peaks due to the azo-linkage or the bonds in the vicinity of this linkage are not detected after dark adsorption. However, we may suggest that the absence of the bands at 1198 cm^{-1} (symmetric SO$_3$ vibration) and 1304 cm^{-1} (asymmetric SO$_3$ vibration) may evidence the adsorption of MO molecule on the supported catalyst surface via oxygen atoms of sulfonate group. Stylidi et al. and Ökte et al. proposed similar mechanisms for the adsorption of AO7 molecule on TiO$_2$ surface and the adsorption of MO molecule on the lanthanum loaded TiO$_2$ supported ZSM-5 photocatalysts, respectively [58,59]. Concluding and excluding the MO's spectra, the major constituents in all the IR patterns, are essentially due to the silica and alumina framework of the support. Therefore, the vibrations of the bonds corresponding to other phases (such as ZnO catalyst and MO molecule) overlap and render the peaks deconvolution and interpretation of the patterns more difficult in terms of their appearance and/or significance in the resultant catalyst matrix.

3.1.7. UV–vis DRS analysis

Fig. 9 presents UV–vis absorption spectroscopies and band gap adsorption edges of the raw FA, 0.25 M ZnO and the supported catalysts. The raw FA shows an extending absorption tail in between
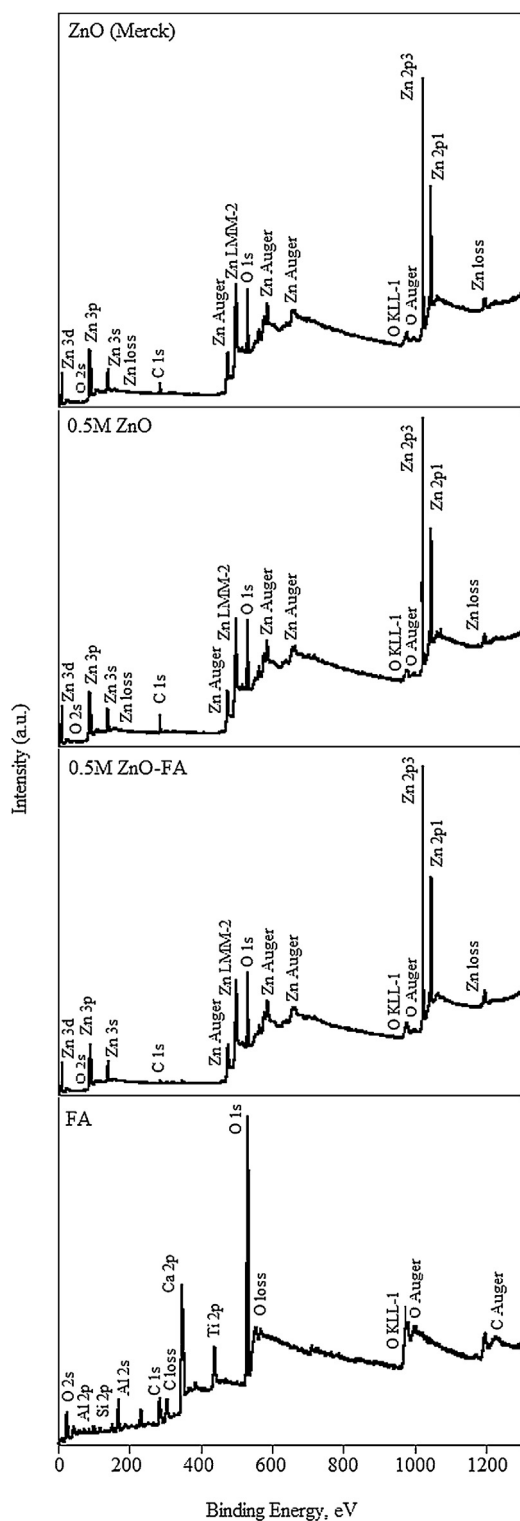
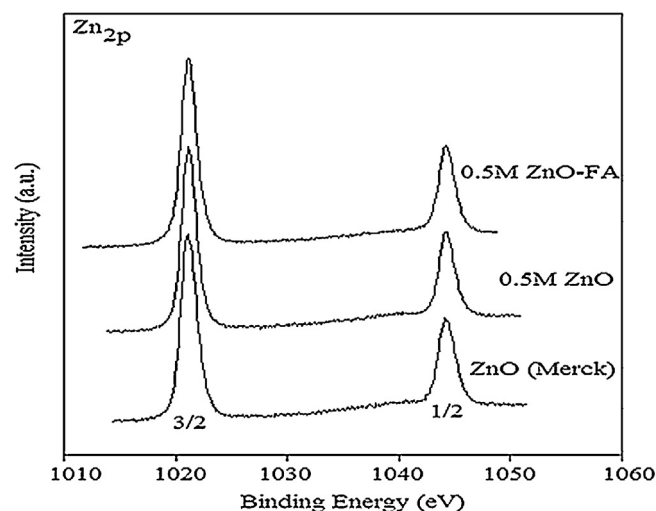**Fig. 5.** XPS survey analysis: FA, 0.5 M ZnO-FA, 0.5 M ZnO and ZnO (Merck).

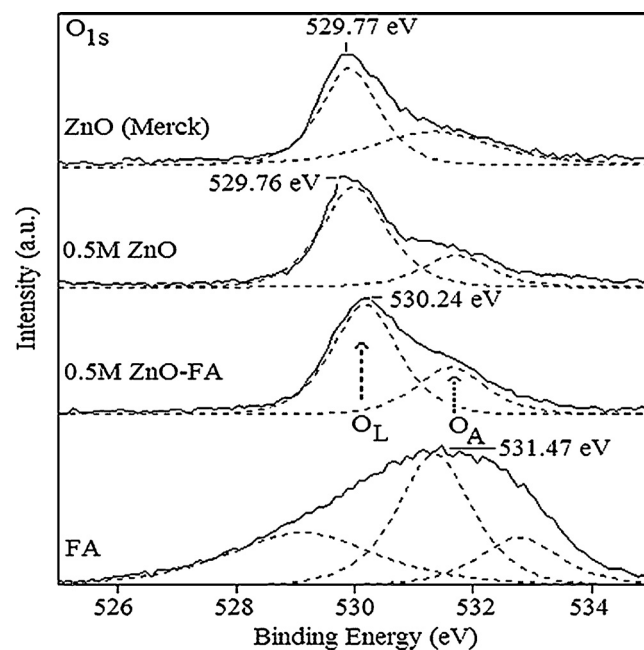**Fig. 6.** Zn 2p XPS spectra of ZnO (Merck), 0.5 M ZnO and 0.5 M ZnO-FA.

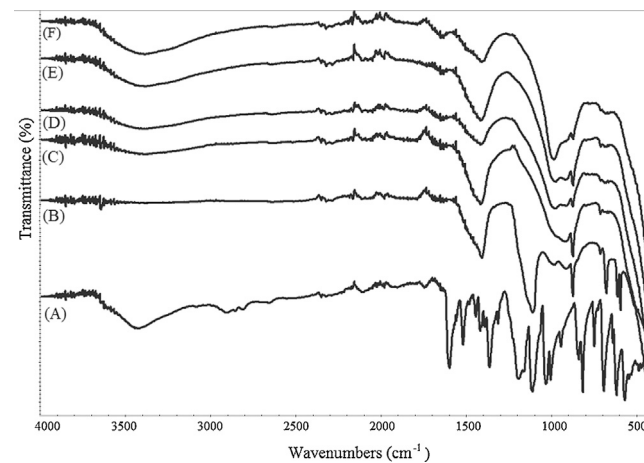**Fig. 7.** O 1s XPS spectra of FA, 0.5 M ZnO-FA, 0.5 M ZnO and ZnO (Merck).

Fig. 8. FTIR spectra of (A) MO, (B) FA, (C) 0.25 M ZnO-FA, (D) 0.25 M ZnO-FA (after dark adsorption), (E) 0.25 M ZnO-FA (after 1st irradiation cycle) and (F) 0.25 M ZnO-FA (after 4th irradiation cycle).
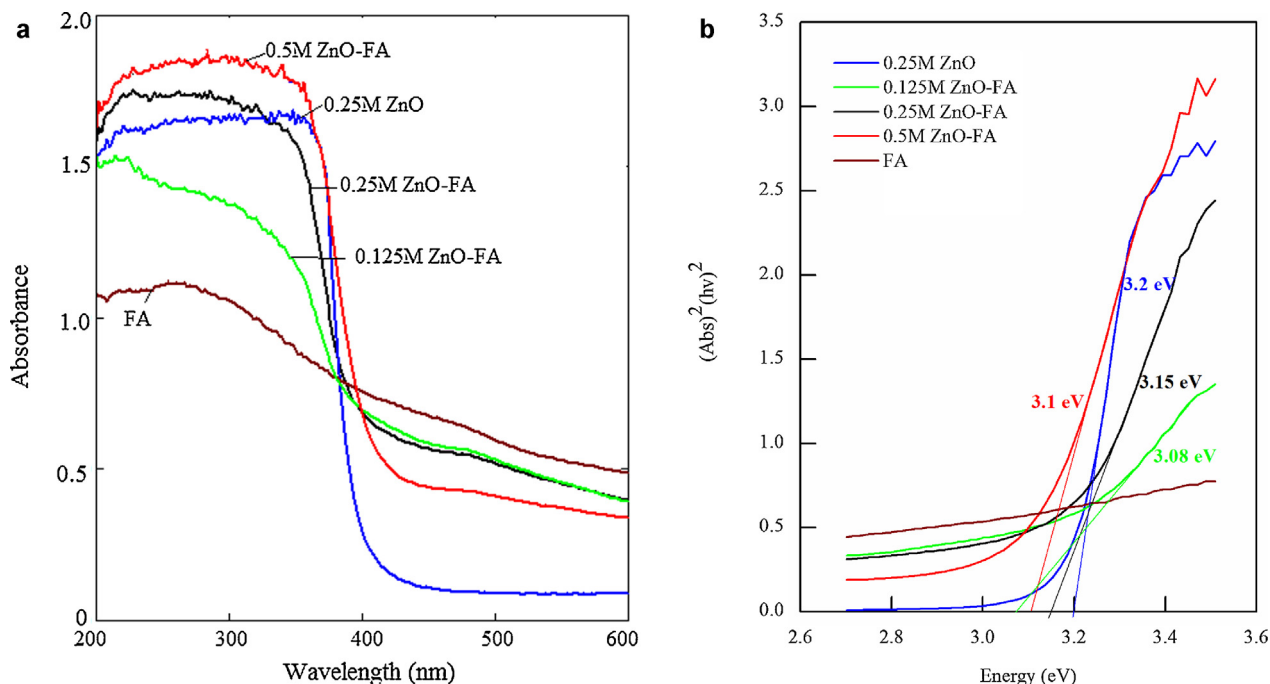
200 nm and 600 nm (Fig. 9a). All ZnO loaded FA catalysts exhibit the characteristic sharp absorption edge of ZnO and their absorption profiles increase with the loading concentration of ZnO in the low wavelength regions (below 380–390 nm). Around 380–390 nm, the absorption edges of all supported catalysts shift slightly to the longer wavelength regions in comparison to 0.25 M ZnO due to the existence of FA in the composite structure. In addition, the UV–vis absorption spectra of the as prepared catalysts are transformed to

Fig. 9. (a) UV–vis DRS spectra and (b) band gap adsorption edges of FA, 0.25 M ZnO, 0.125 M ZnO-FA, 0.25 M ZnO-FA and 0.5 M ZnO-FA.

the band-gap values which are evaluated by linear extrapolation and taking the intercept on the *x*-axis gives the value of the band gap (Fig. 9b). A slight decrease is observed for the supported catalysts in comparison to the 0.25 M ZnO, without detection of any systematic variation among them.

3.2. Adsorption and photocatalytic applications

3.2.1. Water vapor adsorption

The hydrophilicity of the supported nanocatalysts is investigated by the water vapor adsorption isotherms. From very low relative humidity, the water vapor adsorption at the ZnO-FA composites is higher than the raw FA and the differences increase with increasing relative humidity (Fig. 10). The isotherm of the fly ash sample is of type III indicating the hydrophobicity of the material with chemisorption rather than physical sorption and monolayer sorption even at high relative pressure. In contrast, water vapor isotherms of the ZnO-FA composites show a type IV behavior due to the transformation of the hydrophobic fly ash to a hydrophilic mesoporous ZnO-FA with capillary condensation at high relative humidity. In addition, ZnO nanoparticles contributes to the high determined values since a jump in its water vapor adsorption isotherm (type II behavior) at around 80% of relative humidity is expected and the increase to 0.08 g of sorbed water vapor per g of ZnO particles at 93% of relative humidity [60]. This effect contributes also to the higher values obtained for the 0.5 M ZnO-FA in comparison to the 0.25 M ZnO-FA, complementary to the creation of more porous active sites upon ZnO formation on the cenospheres surfaces. Moreover, the hydrophilic behavior of the mesoporous nano-composite is evident for calcination temperatures of the composite from 300 °C and up to 500 °C. Therefore, the prepared nano-composite can be also used as a thermo-responsive and solar cooling material for the utilization of the water vapor absorption resonances and continuum in the visible and infrared part of the solar radiation spectrum in addition to the photodegradation applications.

3.2.2. Photolysis and dark adsorption experiments

Two sets of initial experiments were designed prior to the photocatalytic degradation studies. The first set involved photolysis of MO and dark experiments over the raw FA and 0.25 M ZnO catalyst (Fig. 11). A negligible degradation is observed in the presence of UV light without any catalyst. The percentages of MO remaining in the solution are found as 91.5% at 278 nm and 85.6% at 464 nm in the presence of only FA. However, 0.25 M ZnO demonstrates
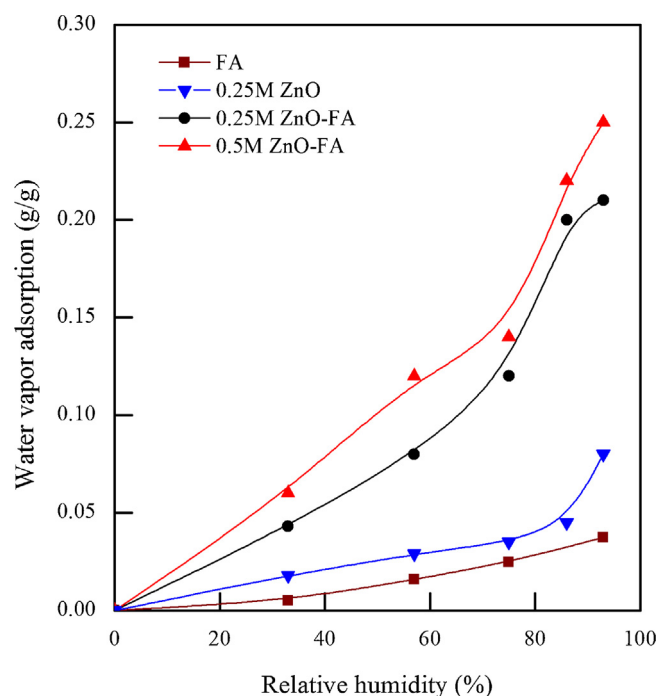

Fig. 10. Water vapor adsorption isotherms of FA, 0.25 M ZnO, 0.25 M ZnO-FA and 0.5 M ZnO-FA.
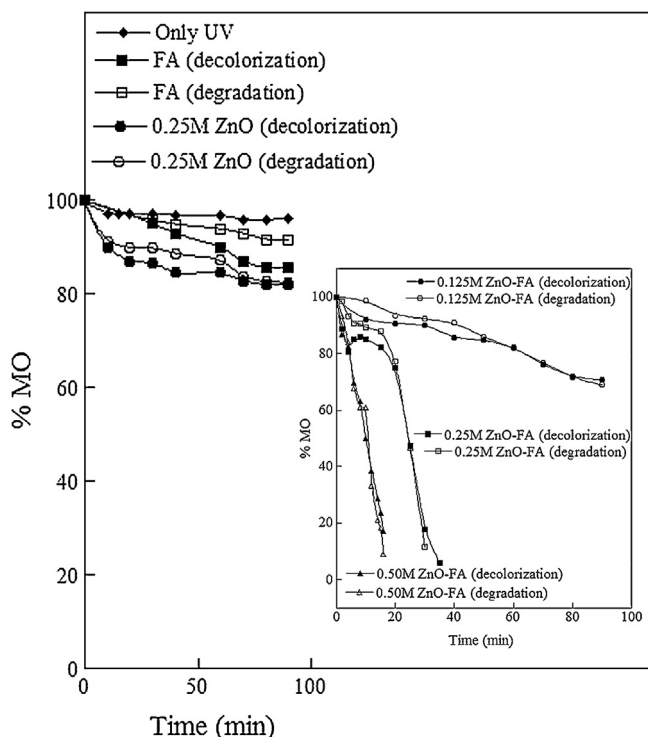
Fig. 11. Results of photolysis and dark adsorption experiments in the presence of FA and 0.25 M ZnO. Inset: Dark adsorption experiments in the presence of supported nanocatalysts.

relatively lower percentages, indicating a better adsorption capacity in comparison to the raw support. After 90 min mixing in the dark, no significant change is noticed in the MO percentages.

The second set of control experiments investigated dark adsorption capacities of the supported nanocatalysts (Fig. 11 inset). The existence of ZnO nanoparticles on the FA matrix improves the adsorption ability. This is pronounced with an increase in the loading concentration of ZnO. Besides, adsorption proceeds in shorter periods for the catalysts involving higher concentrations of ZnO. In the presence of 0.125 M ZnO-FA, around 70% MO is detected in the reaction media after 90 min. In the presence of the 0.25 M ZnO-FA and 0.5 M ZnO-FA catalysts, 11% MO after 35 min and 9% after 16 min remain in the solution, respectively. Consequently, ZnO loading on the FA material has superior adsorption properties for the MO removal from aqueous solutions. This significant FA transformation is observed for the first time and is analogous to its alteration to a porous material under time and energy consuming alkaline treatments [48]. It can be attributed to the porosity creation with the in situ build up of ZnO nanoparticles on the FA cenospheric surfaces. This result is corroborated from the SEM, XPS and nitrogen–water vapor adsorption isotherms described in the previous sections. Therefore, the as-prepared supported nanocatalysts could be potentially utilized as adsorbers in the absence or limited illumination.

3.2.3. Adsorption kinetics and adsorption isotherms

Adsorption kinetic experiments were investigated to study adsorption details of MO on the 0.5 M ZnO-FA catalyst (Fig. 12). Since it is difficult to establish adsorption equilibrium for the lower initial concentrations of MO, the highest initial MO concentration, $32.7 \, \text{mg L}^{-1}$ ($0.1 \, \text{mmol L}^{-1}$) is selected for the application of two well known adsorption models, pseudo-first and pseudo-second order equations.

The amount of MO adsorbed per gram of adsorbent (0.5 M ZnO-FA) at time t (min) can be found by the following equation [61,62]

$$q_t = \frac{(C_0 - C_t)V}{m} \tag{3}$$

where q_t (mmol g^{-1}) is the amount of adsorbed MO per gram of adsorbent at time t (min), C_0 is the initial concentration of MO in solution (mmol L^{-1}), C_t is the concentration of MO (mmol L^{-1}) at time t (min), V is the volume of the solution (L) and m is the mass of the supported catalyst used (g). In case C_t is replaced with C_e (concentration of MO at equilibrium), q_e (mmol g^{-1}) is calculated instead of q_t as the amount of adsorbed MO per gram of adsorbent at equilibrium.

The pseudo-first order equation is

$$\frac{dq_t}{dt} = k_1(q_e - q_t) \tag{4}$$

where k_1 is the pseudo-first order rate constant (min). After integration of the equation by using integral limits of $q_t = 0$ at $t = 0$ and $q_t = q_t$ at $t = t$, Eq. (4) becomes

$$\ln(q_e - q_t) = \ln q_e - k_1 t \tag{5}$$

The plot of $\ln(q_e - q_t)$ versus t should give a straight line (Fig. 12a). The rate constant (k_1) can be calculated from the slope of this line. Our experimental data fits the pseudo-first order analysis with 0.9171 (for degradation) and 0.9150 (for decolorization) correlation coefficients.

The pseudo-second order equation is given by the following equation

$$\frac{dq_t}{dt} = k_2(q_e - q_t)^2 \tag{6}$$

After the integration of the equation by the integral limits of $q_t = 0$ at $t = 0$ and $q_t = q_t$ at $t = t$, Eq. (6) becomes

$$\frac{t}{q_t} = \left(\frac{1}{k_2 q_e^2}\right) + \frac{t}{q_e} \tag{7}$$

The linearity obtained in the plot of t/q_t versus t results in 0.9958 (for degradation) and 0.9967 (for decolorization) correlation coefficients (Fig. 12b). The higher values of the coefficients imply a better adsorption of MO on the supported nanocatalyst by using the pseudo-second order model while only a certain extent of adsorption seems to be possible by the application of the pseudo-first order model.

For the adsorption isotherms, Freundlich and Langmuir models are employed at five different initial concentrations of MO (32.7, 16.3, 8.17, 3.27 mg L^{-1}). The linearized form of the Freundlich isotherm is given as follows [61–63]

$$\ln q_e = \ln K_F + b_F \ln C_e \tag{8}$$

where K_F is the Freundlich constant and b_F is the adsorption intensity constant. The line fittings of $\ln q_e$ versus $\ln C_e$ plots give 0.6473 (for degradation) and 0.9288 (for decolorization) correlation coefficients (Fig. 12c).

The form of Langmuir isotherm is as follows

$$\frac{C_e}{q_e} = \frac{C_e}{q_{max}} + \frac{1}{q_{max} K_L} \tag{9}$$

where q_{max} (mmol g^{-1}) is the maximum capacity of the adsorbent and K_L (L mmol^{-1}) is the Langmuir adsorption constant (Fig. 12d). The linearity obtained in the plots of C_e/q_e versus C_e for both degradation and decolorization processes results in higher correlation coefficients; 0.9951 and 0.9943, respectively (Fig. 12d). Therefore, the adsorption of MO on the 0.5 M ZnO-FA catalyst fit with the
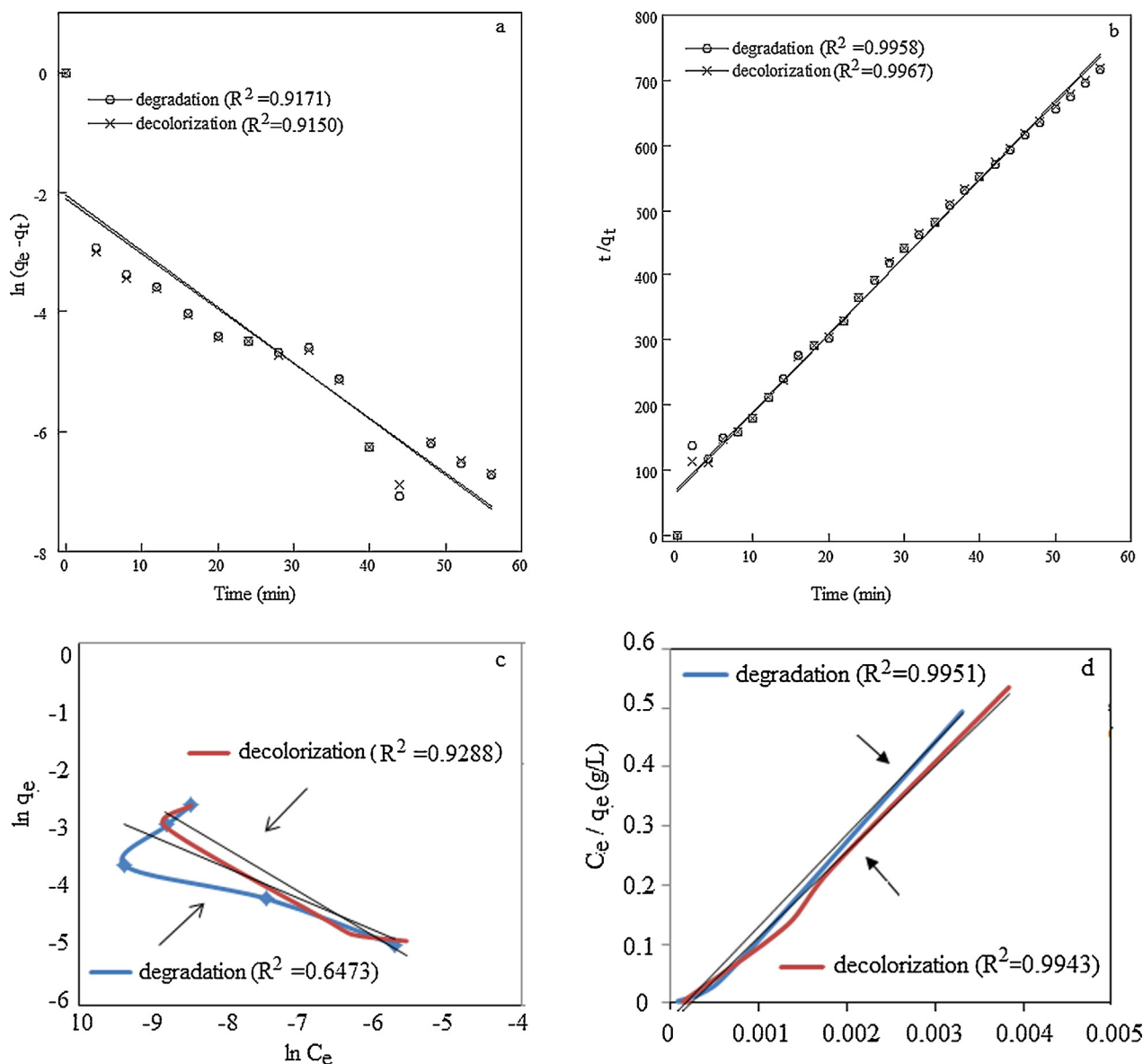
Fig. 12. Results of adsorption kinetics and isotherm models for adsorption of MO on 0.5 M ZnO-FA. (a) Pseudo-first order kinetics, (b) pseudo-second order kinetics, (c) Freundlich model and (d) Langmuir model.

Langmuir model better than the Freundlich model. This also indicates the monolayer coverage on the support surface. From the slope of the lines, Langmuir adsorption capacities are calculated as 2.05 mg g^{-1} and 2.25 mg g^{-1} for degradation and decolorization processes, respectively.

3.2.4. Photocatalytic activity

Photodegradation experiments were subsequently performed in the presence of 0.25 M ZnO, 0.5 M ZnO and all supported nanocatalysts under UV irradiation (Fig. 13). Since dark adsorption capacities of the supported nanocatalysts were quite high for the 0.25 M ZnO-FA and 0.5 M ZnO-FA samples, the short period of 2 min was selected for the mixing of 0.125 M ZnO-FA, 0.25 M ZnO-FA and 0.5 M ZnO-FA with MO in the dark. In contrast, 30 min contact of MO was applied to 0.25 M ZnO and 0.5 M ZnO catalysts under dark. As a general remark of the experiments carried out under irradiation, all catalysts reveal very good photocatalytic activities with fast decolorization and degradation rates. Among the supported catalysts, the lowest MO remaining percentages with slower rates are obtained in the presence of 0.125 M ZnO-FA while

the best performance is exhibited by the 0.5 M ZnO-FA catalyst with almost total MO degradation in less than 10 min. Similar to the dark experiments, higher concentrations of ZnO in the final catalyst composition (either supported or unsupported forms of the catalysts) improved the photocatalytic efficiencies. Moreover, even though weight percentages of Zn are much lower in absolute values in the supported nanocatalysts based on the XRF measurements (73.5% Zn in 0.25 M ZnO, 24.1% Zn in 0.25 M ZnO-FA and 35.3% Zn in 0.5 M ZnO-FA, Table 1), both decolorization and degradation rates are greater in the presence of these nanocatalysts relative to their unsupported forms. The following sequence of degradation and decolorization rates are detected:

0.125 M ZnO-FA < 0.25 M ZnO < 0.25 M ZnO-FA

    < 0.5 M ZnO < 0.5 M ZnO-FA

It can be inferred that the combined form of ZnO and FA induces a kind of synergy in comparison to the independent forms. It is this cooperation that introduces the bifunctional properties of the supported catalysts; dark adsorption capability in addition to
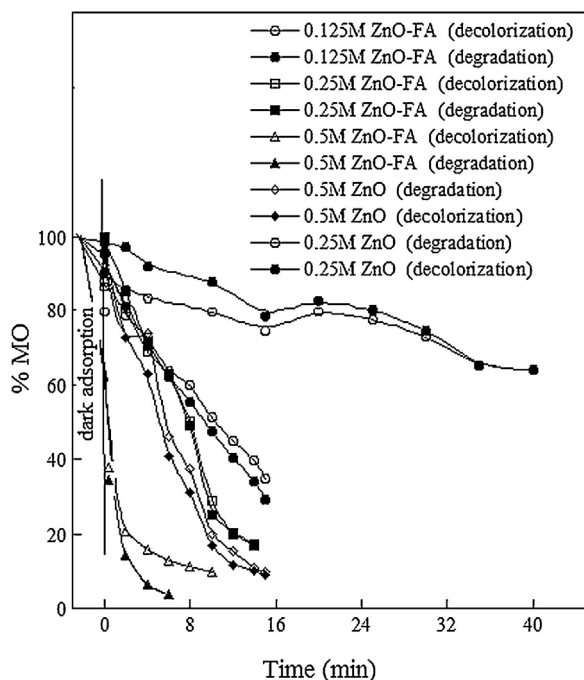
Fig. 13. Degradation and decolorization of MO under irradiation.

photocatalytic activity. Fig. 14 summarizes the results obtained from dark adsorption capacities within 30 min and photocatalytic performances of experiments within 10 min irradiation.

3.2.5. Kinetics and mechanism of photocatalysis

The data from the photocatalytic activities was further used to analyze the rate of reactions. The supported catalysts are examined in the presence of 3.27 mg L^{-1} MO by the following equation

$$R = \frac{dC}{dt} = kC \tag{10}$$
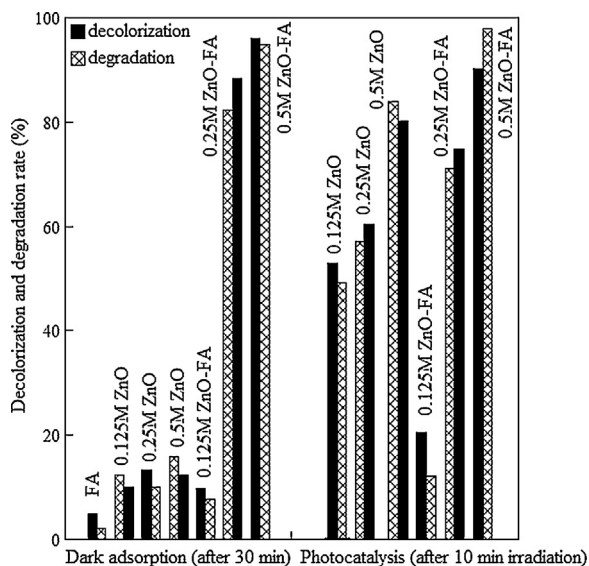
Fig. 14. Degradation and decolorization rate (%) of MO after dark adsorption (30 min) and irradiation (10 min) using FA, 0.125 M ZnO, 0.25 M ZnO, 0.5 M ZnO, 0.125 M ZnO-FA, 0.25 M ZnO-FA and 0.5 M ZnO-FA.
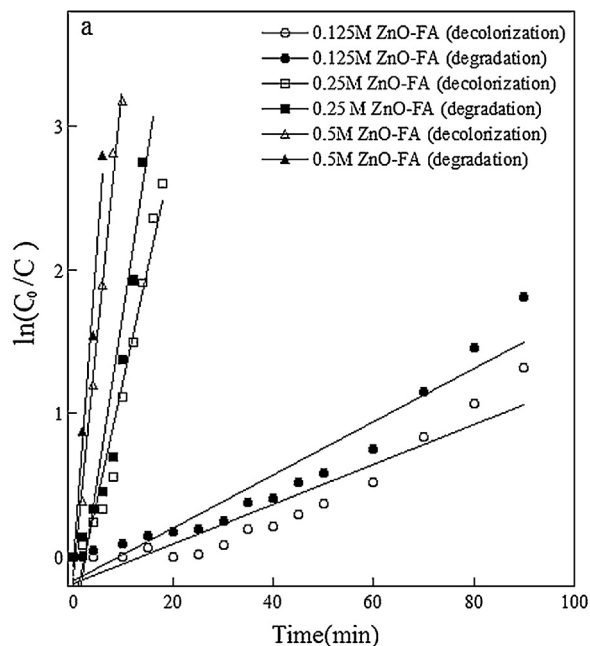

Fig. 15. Kinetic analysis of MO degradation and decolorization under irradiation in the presence of supported catalysts.

where R is the rate of decolorization (or degradation), C is the concentration of MO at time t, k is the rate constant. The equation can be simplified by integration as

$$\ln \frac{C_0}{C} = kt \tag{11}$$

where C_0 is taken as the equilibrium concentration of MO (mg L^{-1}) after dark adsorption. The obtained linearity in the plot of $\ln(C_0/C)$ versus t results in pseudo-first-order kinetics (Fig. 15). Hence, the rate-constants (k, min^{-1}) calculated from the slopes of the lines, increase with the loading concentration of ZnO in supported catalysts (Table 5).

The influence of the initial MO concentration varying from 3.27 mg L^{-1} to 32.7 mg L^{-1} on the photocatalytic rate is also investigated in the presence of 0.5 M ZnO-FA (Fig. 16). Pseudo-first-order kinetics is confirmed by the linearity noticed in examined concentration range of MO (Fig. 17). The efficiency of both decolorization and degradation processes is found to decrease with increasing concentration of MO (Table 5). This can be a result of blocking of the photocatalytically active sites on the supported catalyst and reducing the interaction of photons with these sites.

Many researchers have also used Langmuir–Hinshelwood kinetic model to analyze heterogeneous photocatalytic reactions

Table 5
Rate constants (k) and linear regression values (R) of the supported catalysts for decolorization and degradation processes. 3.27 mg L^{-1} MO was used in the kinetics analysis of the supported catalysts.

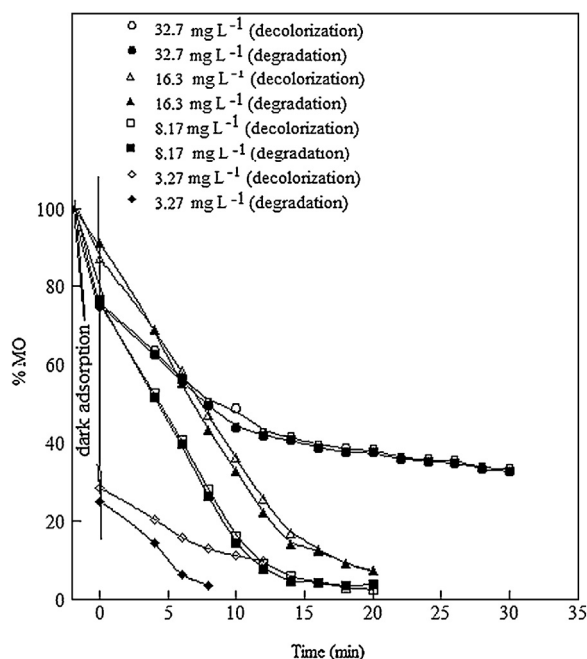| Catalysts	k (min^{-1})$^{a/b}$	$R^{a/b}$
0.125 M ZnO-FA	0.013/0.018	0.940/0.960
0.25 M ZnO-FA	0.156/0.225	0.976/0.944
0.5 M ZnO-FA	0.341/0.454	0.993/0.991
[MO] (mg L^{-1})	k (min^{-1})$^{a/b}$	$R^{a/b}$
32.7	0.055/0.057	0.950/0.942
16.3	0.153/0.173	0.994/0.994
8.17	0.251/0.274	0.998/0.998
3.27	0.341/0.454	0.993/0.991

a/b: decolorization/degradation.

Fig. 16. Effect of different initial MO concentrations in the presence of 0.5 M ZnO-FA.

in terms of the concentration of the target molecule [11,63,64]. The model is also rationalized for our experimental results by the following equation

$$R = \frac{kKC}{1 + KC} = k_{app}C \tag{12}$$

This equation can be rearranged as

$$\frac{1}{R} = \frac{1}{kKC} + \frac{1}{k} \tag{13}$$

where R is the rate of decolorization, K is the adsorption coefficient of MO onto the supported catalyst (L mg^{-1}), and k is the reaction rate constant (mg L^{-1} min^{-1}). The applicability of Langmuir–Hinshelwood equation for the decolorization and degradation processes has been confirmed by the linearity in the plot of reciprocal of rate $(1/R)$ against reciprocal of initial MO concentration $(1/C_0)$ (Fig. 17 inset). The values of K and k are found to be 0.112 L mg^{-1} and 4.17 mg L^{-1} min^{-1} (for decolorization) and 0.191 L mg^{-1} and 3.82 mg L^{-1} min^{-1} (for degradation).
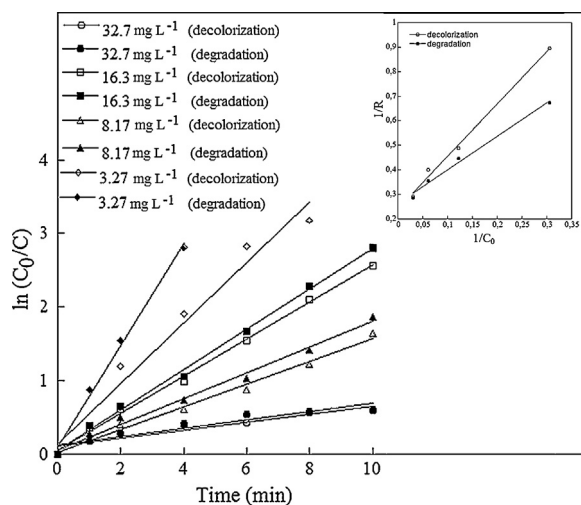

Fig. 17. Linearized kinetic plot. Inset: Langmuir–Hinshelwood plot.

The photocatalytic degradation mechanism starts with the illumination of ZnO nanoparticles and production of electron–hole pairs (Eq. (14)).

$$ZnO + h\gamma(UV) \rightarrow e_{CB}^- + h_{VB}^+ \tag{14}$$

For the efficiency of the process, inhibition of electron–hole pair recombination is required. Thus, electrons and holes should be captured by any chemical species existing on the surface or by the so-called surface traps as also mentioned in the study of Zawadzki for TiO$_2$ systems [65,66].
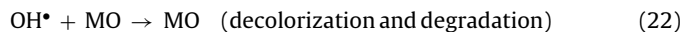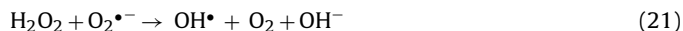
The valence band hole (h_{VB}^+) is positively enough for the direct (Eq. (15)) and indirect oxidation of MO via hydroxyl radicals (Eqs. (16)–(17)).

$$h^+ + MO \rightarrow MO^{\bullet+} \rightarrow MO \quad \text{(decolorization and degradation)} \tag{15}$$
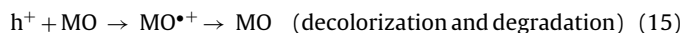
Hydroxyl radicals can be generated when the surface adsorbed water or hydroxyl anions react with the holes (Eqs. (16) and (17))

$$h^+ + H_2O \rightarrow OH^\bullet + H^+ \tag{16}$$

$$h^+ + OH^- \rightarrow OH^\bullet \tag{17}$$

An alternative route for the production of OH$^\bullet$ radicals is the formation of superoxide radicals with electrons (Eq. (18)). Superoxide radicals are known as oxidizing agents and contribute to the formation of hydrogen peroxide via hydroperoxyl radical generation (Eqs. (19)–(22)) [67].

$$O_2 + e^- \rightarrow O_2^\bullet \tag{18}$$

$$O_2^{\bullet-} + H^+ \rightarrow HO_2^\bullet \tag{19}$$

$$2HO_2^\bullet \rightarrow H_2O_2 + O_2 \tag{20}$$

$$H_2O_2 + O_2^{\bullet-} \rightarrow OH^\bullet + O_2 + OH^- \tag{21}$$

$$OH^\bullet + MO \rightarrow MO \quad \text{(decolorization and degradation)} \tag{22}$$

Major role of all these radicals is to react with the MO molecule and disrupt it in its conjugated system. This eventually leads to the complete decomposition. Among the radicals formed, OH$^\bullet$ radicals are known as highly reactive electrophilic oxidants. Their presence whether from the route of holes or electrons accelerates the decolorization and degradation mechanism of the MO molecule. The main reaction pathway (60%) is the addition of the hydroxyl radical to the double bond of the azo group, resulting in the rapid disappearance of color; however, addition to the aromatic ring also occurs (40%) [68,69]. Addition of a hydroxyl radical to the carbon atom bearing the azo bond was proposed by Spadaro et al. [69]. Thereafter, breaking of the adduct could form benzenesulfonoic acid, N,N-dimethylaniline and 4-hydroxy-N,N-dimethylaniline [70,71]. Further OH$^\bullet$ attacks cause the identification of sulfonated intermediates, aromatic amine and phenolic compounds [47]. This is followed by open ring fragments and generation of inorganic final products such as SO$_4^{2-}$, NO$_3^-$, NH$_4^+$, CO$_2$ and H$_2$O [59,72].

3.2.6. Reuse properties

Reusing properties of the supported nanocatalysts were investigated in recycling experiments (Fig. 18). In general, particle filtration arises as a major problem whenever ZnO is utilized alone as a photocatalyst. According to Shi et al. [36], an analogous difficulty existed in the as-prepared TiO$_2$ powder and P25 samples. Even though these catalysts are more effective in the depigmentation of MO molecules, TiO$_2$ added coal fly ash is used to minimize the problems in the filtration step. Besides, cleaning and recycling
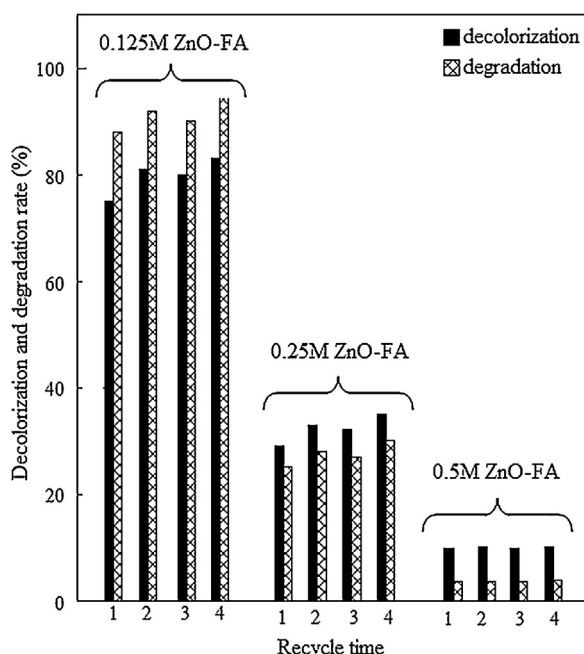
Fig. 18. Results of recycling studies in the presence of supported nanocatalysts.

of the powder catalysts in the absence of supports are impracticable in large scale applications [36]. Thus, reuse properties of the ZnO loaded FA nanocatalysts were determined. For each new cycle, the photocatalyst is filtrated, washed and calcined at 500 °C for 2 h by keeping constant the other reaction conditions. After four cycles, the percentage of MO remaining in the solution is found to increase only approximately 2–3% in the presence of both 0.125 M ZnO-FA and 0.25 M ZnO-FA. The lowest increments are detected as 0.2–0.4% for 0.5 M ZnO-FA. The insignificant loss of photoactivity can be explained either by the presence of reaction by-products adsorbed on the photocatalyst after the first run, decreasing the MO removal in the following runs or by the loss of the photocatalysts during each collection and rinsing steps. Moreover, SEM images of 0.25 M ZnO-FA (after dark adsorption of MO (Fig. S1) and also after 1st–4th irradiation cycles (Fig. S2 and S3)) and elemental compositions (Table 1) do not reveal an obvious variation in comparison to the image and composition of the same catalyst given in Fig. 4 and Table 1. This also points out the stability and reuse property of the supported catalyst.

4. Conclusion

A novel supported nano-catalyst has been prepared by the buildup of ZnO semiconducting particles on the cenospheres and bulk surfaces of FA. This new material shows bifunctional properties with adsorption capability in addition to photocatalytic activity. Enhanced adsorption of MO and water vapor on the supported catalysts compared to ZnO was determined. By extensive characterization techniques, the pronounced performance was attributed to the transformation of FA to a mesoporous structure. Improved photocatalytic efficiencies were obtained by the application of the supported nano-catalysts. The slight shift observed in the bandgap absorption edges of the supported catalysts implies the possibility to extent the photocatalytic applications in the visible range. Combined with the water vapor adsorption and the utilization of the IR part of the solar spectrum open up new opportunities and widens the application prospects of the prepared nanocatalysts.

Appendix A. Supplementary data

Supplementary data associated with this article can be found, in the online version, at http://dx.doi.org/10.1016/j.plantsci.2004.08.011.

References

[1] A. Dhakshinamoorthy, S. Navalon, A. Corma, H. Garcia, Energy & Environmental Science 5 (2012) 9217–9233.
[2] B. Swarnalata, Y. Anjaneyulu, Journal of Molecular Catalysis A: Chemical 223 (2004) 161–165.
[3] A. Akyol, M. Bayramoglu, Journal of Hazardous Materials B 124 (2005) 241–246.
[4] M.J. Height, S.E. Pratsinis, O. Mekasuwandumrong, P. Praserthdam, Applied Catalysis B: Environmental 63 (2006) 305–312.
[5] C.C. Chen, Journal of Molecular Catalysis A: Chemical 264 (2007) 82–92.
[6] C.C. Chen, C.S. Lu, Environmental Science & Technology 41 (2007) 4389–4396.
[7] T.J. Kuo, C.N. Lin, C.L. Kuo, M.H. Hung, Chemistry of Materials 19 (2007) 5143–5147.
[8] A.H. Akyol, C. Yatmaz, M. Bayramoblu, Applied Catalysis B: Environmental 54 (2004) 19–24.
[9] C.C. Chen, Journal of Molecular Catalysis A: Chemical 264 (2006) 82–92.
[10] K. Hayata, M.A. Gondalb, M.M. Khaleda, S. Ahmed, A.M. Shemsi, Applied Catalysis A: General 393 (2011) 122–129.
[11] P.S. Suchithra, C.P. Shadiya, A. Peer Mohamed, P. Velusamy, S. Ananthakumar, Applied Catalysis B: Environmental 130–131 (2012) 44–53.
[12] M.S. Vohra, K. Tanaka, Water Research 37 (2003) 3992–3996.
[13] H. Chen, S.W. Lee, T.H. Kim, B.Y. Hur, Journal of the European Ceramic Society 26 (2006) 2231–2239.
[14] C.H. Ao, S.C. Lee, J.C. Yu, Journal of Photochemistry and Photobiology A 156 (2003) 171–179.
[15] E.P. Melian, O.G. Díaz, J.M.D. Rodríguez, G. Colón, J. Araña, J.H. Melian, J.A. Navío, J.P. Peña, Applied Catalysis A: General 364 (2009) 174–181.
[16] S.J. So, H.J. Kim, H. du Cha, C.S. Han, Journal of Nanoscience and Nanotechnology 11 (2011) 850–857.
[17] M. Takeuchi, T. Kimura, M. Hidaka, D. Rakhmawaty, M. Anpo, Journal of Catalysis 246 (2007) 235–240.
[18] H. Yahiro, T. Miyamoto, N. Watanabe, H. Yamaura, Catalysis Today 120 (2007) 158–162.
[19] W. Panpa, P. Sujaridwokarun, S. Jinawath, Applied Catalysis B: Environmental 80 (2008) 271–276.
[20] N. Dubey, S.S. Rayalu, N.K. Labhsetwar, R.R. Naidu, R.V. Chatti, S. Devotta, Applied Catalysis A: General 303 (2006) 152–157.
[21] K. Shimizu, T. Kaneko, T. Fujishima, T. Kodama, H. Yoshida, Y. Kitayama, Applied Catalysis A: General 225 (2002) 185–191.
[22] A.N. Ökte, E. Sayinsöz, Separation and Purification Technology 62 (2008) 535–543.
[23] Y. Xu, C.H. Langford, Journal of Physical Chemistry B 101 (1997) 3115–3121.
[24] J.M. Lopez Nieto, Topics in Catalysis 15 (2001) 189–194.
[25] M. Santamouris, Advanced Building Energy Research 1 (2007) 123–150.
[26] E. Vardoulakis, D. Karamanis, M.N. Assimakopoulos, G. Mihalakakou, Solar Energy Materials and Solar Cells 95 (2011) 2363–2370.
[27] D. Karamanis, E. Vardoulakis, E. Kyritsi, N. Ökte, Energy Conversion and Management 63 (2012) 118–122.
[28] A.X. Zeng, W.H. Xiong, J. Xu, Surface and Coatings Technology 197 (2005) 142–147.
[29] J. Lu, F. Xu, D.J. Wang, J. Huang, W.M. Cai, Journal of Hazardous Materials 165 (2009) 120–125.
[30] W. Liu, X.Q. Shen, D.H. Li, Powder Technology 186 (2008) 273–277.
[31] Y. Yu, Powder Technology 146 (2004) 154–159.
[32] M. Visa, R.A. Carcel, L. Andronic, A. Duta, Catalysis Today 144 (2009) 137–142.
[33] P. Huo, Y. Yan, S. Li, H. Li, W. Huang, Applied Surface Science 255 (2009) 6914–6917.
[34] P. Huo, Y. Yan, S. Li, H. Li, W. Huang, Applied Surface Science 256 (2010) 3380–3385.
[35] P. Huo, Y. Yan, S. Li, H. Li, W. Huang, S. Chen, X. Zhang, Desalination 263 (2010) 258–263.

[36] J. Shi, S. Chen, S. Wang, P. Wu, G. Xu, Journal of Molecular Catalysis A 303 (2009) 141–147.
[37] P. Huo, Y. Yan, S. Li, H. Li, W. Huang, Desalination 256 (2010) 196–200.
[38] J. Shi, S. Chen, S. Wang, Z. Ye, P. Wu, B. Xu, Journal of Molecular Catalysis A 330 (2010) 41–48.
[39] J. Shi, S. Chen, S. Wang, Z. Ye, S. Wang, P. Wu, Applied Surface Science 257 (2010) 1068–1074.
[40] Z. Shi, S. Yao, C. Sui, Catalysis Science & Technology 1 (2011) 817–822.
[41] B. Wang, Q. Li, W. Wang, Y. Li, J. Zhai, Applied Surface Science 257 (2011) 3473–3479.
[42] B. Wang, C. Li, J. Pang, X. Qing, J. Zhai, Q. Li, Applied Surface Science 258 (2012) 9989–9996.
[43] S. Anandan, A. Vinua, K.L.P. Sheeja Lovely, N. Gokulakrishnan, P. Srinivasu, T. Mori, V. Murugesan, V. Sivamurugan, K. Ariga, Journal of Molecular Catalysis A 266 (2007) 149–157.
[44] D. Karamanis, X. Aslanoglou, P.A. Assimakopoulos, N.H. Gangas, Nuclear Instruments and Methods in Physics Research Section B 181 (2001) 616–621.
[45] K.T. Chung, Mutation Research 114 (1983) 269–281.
[46] K.T. Chung, S.E. Stevens Jr., C.E. Cernigla, Critical Reviews in Microbiology 18 (1992) 175–190.
[47] C. Galindo, P. Jacques, A. Kalt, Journal of Photochemistry and Photobiology A: Chemistry 130 (2000) 35–47.
[48] X. Querol, F. Plana, A. Alastuey, A. Lopez-Soler, Fuel 76 (1997) 793–799.
[49] K.S.W. Sing, D.H. Everett, R.A.W. Haul, L. Moscou, R.A. Pierotti, J. Rouquerol, T. Siemieniewska, Pure and Applied Chemistry 57 (1985) 603–619.
[50] L. Jing, Z. Xu, X. Sun, J. Shang, W. Cai, Applied Surface Science 180 (2001) 308–314.
[51] O. Lupan, L. Chow, G. Chai, B. Roldan Cuenya, A. Naitabdi, A. Schulte, H. Heinrich, Materials Science and Engineering: B 145 (2007) 57–66.
[52] O. Lupan, G.A. Emelchenko, V.V. Ursaki, G. Chai, A.N. Redkin, A.N. Gruzintsev, I.M. Tiginyanu, L. Chow, L.K. Ono, B. Roldan Cuenya, H. Heinrich, E.E. Yakimov, Materials Research Bulletin 45 (2010) 1026–1032.
[53] J. Liqiang, W. Dejun, W. Baiqi, L. Shudan, X. Baifu, F. Honggang, S. Jiazhong, Journal of Molecular Catalysis A 244 (2006) 193–200.
[54] V. Crist, PDF Handbooks of Monochromatic XPS Spectra, XPS International LCC, Mountain View, CA, 2005.
[55] Y. Lai, M. Meng, Y. Yu, Applied Catalysis B: Environmental 100 (2010) 491–501.
[56] J.C. Vickerman, I.S. Gilmore, B.D. Ratner, D.G. Castner, in: B.D. Ratner, D.G. Castner (Eds.), Electron Spectroscopy for Chemical Analysis, John Wiley and Sons, 2009, pp. 42–95.
[57] D. Panias, I.P. Giannopoulou, Acta Metallurgica Slovaca 12 (2006) 321–327.
[58] M. Stylidi, D.I. Kondarides, X.E. Verykios, Applied Catalysis B: Environmental 47 (2004) 189–201.
[59] A.N. Ökte, Ö. Yılmaz, Applied Catalysis A: General 354 (2009) 132–142.
[60] D.E. Wurster, E. Oh, J.C.T. Wang, Journal of Pharmaceutical Sciences 84 (1995) 1301–1307.
[61] M. Zhou, X. Gao, Y. Hu, J. Chen, X. Hu, Applied Catalysis B: Environmental 138–139 (2013) 1–8.
[62] L. Zhou, C. Gao, W. Xu, ACS Applied Materials & Interfaces 2 (2010) 1483–1491.
[63] S.H. Kim, H.H. Ngo, H.K. Shon, S. Vigneswaran, Separation and Purification Technology 58 (2008) 335–342.
[64] K. Hayat, M.A. Gondal, M.M. Khaled, S. Ahmed, A.M. Shemsi, Applied Catalysis A: General 393 (2011) 122–129.
[65] N. Morales-Flores, U. Pal, E. Sánchez Mora, Applied Catalysis A: General 394 (2011) 269–275.
[66] P. Zawadzki, A.B. Laursen, K.W. Jacobsen, S. Dahl, J. Rossmeisl, Energy & Environmental Science 5 (2012) 9866–9969.
[67] M. Bizarro, Applied Catalysis B: Environmental 97 (2010) 198–203.
[68] J.M. Joseph, H. Destaillats, H. Hung, M.R. Hoffmann, Journal of Physical Chemistry A 104 (2000) 301–307.
[69] J.T. Spadaro, L. Isabelle, V. Renganathan, Environmental Science & Technology 28 (1994) 1389–1393.
[70] K.I. Konstantinou, T.A. Albanis, Applied Catalysis B: Environmental 49 (2004) 1–14.
[71] C. Baiocchi, M.C. Brussino, E. Pramauro, A.B. Prevot, L. Palmisano, G. Marcì, International Journal of Mass Spectrometry 214 (2002) 247–256.
[72] A.N. Ökte, Ö. Yılmaz, Applied Catalysis B: Environmental 85 (2008) 92–102.